Band Gap Tuning of Solution-Processed Ferroelectric Perovskite BiFe$_{1-x}$Co$_x$O$_3$ Thin Films

Pamela Machado, Mateusz Scigaj, Jaume Gazquez, Estel Rueda, Antonio Sánchez-Díaz, Ignasi Fina, Martí Gibert-Roca, Teresa Puig, Xavier Obradors, Mariano Campoy-Quiles, and Mariona Coll*

Institut de Ciència de Materials de Barcelona ICMAB-CSIC, Campus UAB Bellaterra E-08193, Barcelona , Spain

S Supporting Information

ABSTRACT: Ferroelectric perovskite oxides are emerging as a promising photoactive layer for photovoltaic applications because of their very high stability and their alternative ferroelectricity-related mechanism for solar energy conversion that could lead to extraordinarily high efficiencies. One of the biggest challenges so far is to reduce their band gap toward the visible region while simultaneously retaining ferroelectricity. To address these two issues, herein an elemental composition engineering of BiFeO$_3$ is performed by substituting Fe by Co cations, as a means to tune the characteristics of the transition metal−oxygen bond. We demonstrate by solution processing the formation of epitaxial, pure phase, and stable BiFe$_{1-x}$Co$_x$O$_3$ thin films for $x \leq 0.3$ and film thickness up to 100 nm. Importantly, the band gap can be tuned from 2.7 to 2.3 eV upon cobalt substitution while simultaneously enhancing ferroelectricity. As a proof of concept, nonoptimized vertical devices have been fabricated and, reassuringly, the electrical photoresponse in the visible region of the Co-substituted phase is improved with respect to the unsubstituted oxide.
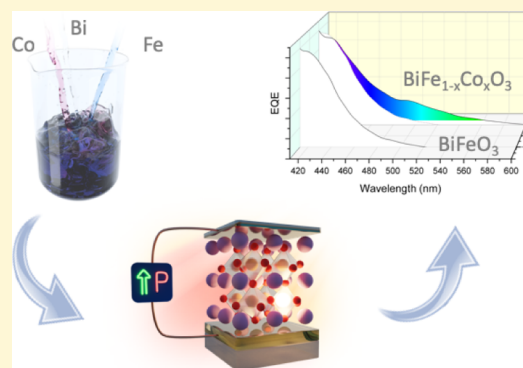
1. INTRODUCTION

All-oxide photovoltaics (PV) is an appealing and versatile approach to help overcome the most persistent challenges in the current PV technologies: to increase the power conversion efficiencies (PCEs) and to lower cost processing with stable and eco-friendly elements. Indeed, oxides are progressively being integrated in solar cells as passivation components, selective layers, and transparent conducting electrodes and to a less extent as light harvesters.[1−4] Recently, semiconductor ferroelectric oxides with a perovskite structure have received a great deal of attention because they can be used as photoactive layers,[5−8] inspired by the rapid increase in PCE (up to 23.7%) of the analogous lead halide perovskites.[9−13] An exceptional property of ferroelectric perovskite oxides is that its non-centrosymmetric structure provides a unique route to spontaneously separate charge carriers, known as bulk photovoltaic effect, achieving extremely large above band gap open-circuit voltages on a single-phase material.[14,15] The aforementioned aspect should allow to speculate that the PCE beyond the Shockley−Queisser limit might be obtained.[16−18] Additionally, they possess a spontaneous electric polarization which allows controlling the direction of the PV current.[19] It is worth to note the high stability at ambient conditions of such metal oxides, as well as their capability to be manufactured by low-cost methodologies.[20] Nonetheless, most of the conventional ferroelectric oxides with a perovskite structure typically absorb in the ultraviolet energy range (band gap $E_g \approx 3−4$ eV, far from the ideal value of ~1.4 eV for the maximum PCE) and

exhibit very low photocurrents at air mass 1.5 global conditions ($1<\mu$A/cm^2).[21,22] The wide band gaps in ferroelectric perovskites, ABO$_3$, are due to a large difference in electronegativity between the transition metal cation (B) and the oxygen (O).[23] Therefore, modifying the B−O bond properties can allow to effectively tune the band gap of the material.[24]

Lowering the E_g and preserving the ferroelectric properties are an appealing route to obtain photovoltaic devices with higher PCE. BiFeO$_3$ (BFO) is among the most attractive lead-free perovskite oxide materials to be used as the photoactive layer in ferroelectric photovoltaic devices. It is a ferroelectric material at room temperature with high saturation polarization along the pseudocubic [111] direction (90 μC/cm^2) and presents a relatively narrow band gap of 2.7 eV.[25] Additionally, having a relatively high index of refraction, n,[26,27] enhances light confinement and, as a result, increases photoabsorption.[28]

Within the various approaches to tune the E_g,[29−32] compositional tuning appears to be one of the most successful.[33−35] Using this approach, a record PCE of 3.3% has been reported in Bi$_2$FeCrO$_6$ (8.1% in multilayer architectures)[23,36] and 4.2% in BiMnO$_3$-based composite films,[37] although they present weaker ferroelectricity than BFO. Despite the fast progress in ferroelectric perovskite oxides, there are still important fundamental issues that need to

be investigated. In particular, efforts to develop new material compositions to lower the band gap and enhance the electrical polarization via cost-effective and scalable processing methods are required. Chemical solution deposition (CSD) is a well-established low-cost route to prepare high-quality multicationic oxides with a wide variety of structural phases including metastable materials.[20,38,39] In particular, CSD has already been used to fabricate epitaxial ferroelectric BFO films.[40,41] Therefore, solution-processed BFO films are an attractive starting point to explore the full potential of band gap tunability via cation substitution for increased solar PCEs at reduced costs.

In this work, we investigate the chemical substitution of the transition metal in CSD-BFO by cobalt ions to judiciously engineer the optical band gap and examine its impact on the ferroelectric properties and the photoresponse. The incorporation of Co in BFO is predicted to display high ferroelectric polarization (P) reaching 170 μC/cm^2 for BiCoO$_3$.[42] Also, the addition of cobalt in BFO can affect the transition metal−oxygen bond characteristics and ultimately the film absorption, a fact that, to the best of our knowledge, has been barely investigated.[43−46] Previous studies showed that the stabilization of BiFe$_{1−x}$Co$_x$O$_3$ (BFCO) phases is limited to a rather narrow growth window requiring high-pressure synthetic conditions.[47,48] Here, we use low-cost and scalable chemical solution to form stable and pure BFCO phase by epitaxial growth with thickness up to 100 nm. Varying stoichiometry enables tuning the band gap from 2.7 to 2.3 eV while preserving a remarkably large polarization P_r = 60 μC/cm^2 at room temperature. Photoresponse measurements at 520 nm show a factor four improvement in the short-circuit current when cobalt is incorporated with respect to the BFO system. This trend is also reflected in the external quantum efficiency (EQE). With this comprehensive study, we demonstrate not only the complexity but also the potential of this system for future light-harvesting applications.

2. EXPERIMENTAL SECTION

2.1. Preparation of BFCO Thin Films. Stoichiometric amounts of hydrated bismuth nitrate, Bi(NO$_3$)$_3$·5H$_2$O, iron nitrate, Fe(NO$_3$)$_3$·9H$_2$O, and cobalt nitrate, Co(NO$_3$)$_2$·6H$_2$O were weighted and dissolved in a solvent blend of 2-methoxyethanol and acetic acid to obtain 0.25 M precursor solutions.[40] When high Co concentrations were added, additional heating (50 °C) and stirring were applied to the precursor solution to obtain a homogeneous solution free of precipitates. The viscosity of all 0.25 M BFCO precursor solution was 0.003 mPa·s. BFCO thin films were prepared from spin-coating 15 μL of BFCO precursor solutions on clean and preheated (70 °C) monocrystalline (001)-strontium titanate (STO) substrates or La$_{0.7}$Sr$_{0.3}$MnO$_3$ (LSMO)-buffered (001) STO substrates at 6000 rpm for 1 min under N$_2$ atmosphere with relative humidity <10%. The spin-coated samples were exposed to a low-temperature thermal treatment at 90 °C for 10 min and then at 270 °C for 4 min. Subsequently, samples were introduced in a preheated tubular furnace at 550−650 °C with a continuous O$_2$ flow of 0.6 l min$^{−1}$ for 30−60 min and quenched to room temperature. This procedure leads to the film thickness of 20 nm. Thicker films (up to 100 nm) were prepared by a multideposition process.

2.2. Preparation of LSMO Thin Films. LSMO metal−organic solution of 0.1 M was prepared from stoichiometric amounts of powder precursors of lanthanum acetate, (CH$_3$COOH)$_3$La, manganese acetate, (CH$_3$COOH)$_2$Mn, and strontium acetate, (CH$_3$COOH)$_2$Sr, dissolved in acetic acid and distilled water. A 15 μL of 0.1 M metal−organic solution was spin-coated on (001)-STO substrates at 6000 rpm for 1 min at ambient atmosphere (35−50% of

humidity) to obtain thin films with a final thickness of ∼10 nm. Subsequently, a crystallization treatment at 900−1000 °C for 10−30 min under O$_2$ atmosphere was performed as described elsewhere (see Figure S7).[49]

2.3. Thin-Film Characterization. *2.3.1. Structure Characterization.* The crystalline structure and phase purity of BFCO films were studied by means of X-ray diffraction (XRD) using Siemens Diffractometer D-5000 with Cu Kα λ = 1.5418 Å for θ−2θ scan analysis in the range 20°−80°. Reciprocal space maps (RSMs) were acquired using Bruker D8 Discover with 2D GADDS (General Area Detector Diffraction System) with Cu Kα λ = 1.5418 Å.

Scanning transmission electron microscopy (STEM) and electron energy loss spectroscopy analysis (EELS) were performed using a Nion UltraSTEM equipment from Oak Ridge National Laboratory, USA, operated at 100 kV and equipped with a fifth-order Nion aberration corrector and an Enfina EEL spectrometer.

2.3.2. Surface Morphology Characterization. Surface morphology and root-mean-square roughness (rms) were studied from topography images acquired from an atomic force microscopy (AFM) Agilent 5100 instrument in dynamic mode.

2.3.3. Optical Characterization. Variable-angle spectroscopic ellipsometry (VASE) measurements were carried out using a SOPRALAB GES5E rotating polarized ellipsometer, which uses a Xe lamp as the light source and a charge-coupled device detector. Ellipsometric spectra were collected at room temperature, and the analyzer was fixed at 20° under different angles of incidence (70°, 72°, and 75°) in the energy range of 1.2−5 eV. Acquired data (ψ and Δ) were analyzed using WinElli II piece of software. The sample was modeled with the structure void/rough layer/bulk film/substrate, and the Tauc−Lorentz model was used to describe the optical properties of the film (see Figure S3). The rough layer assumes a medium consisting of 50% air and 50% film, whose effective dielectric function is modeled using the Bruggeman approximation. The absorption coefficient, α, was calculated from the equation $\alpha = 4\pi\kappa/\lambda$. The film thickness was set to 20 nm, obtained by X-ray reflectometry, and the roughness layer value was varied in each composition according to the AFM analysis (Figure S8).

2.3.4. Surface Chemical Composition Characterization. X-ray photoelectron spectroscopy (XPS) with a Mg Kα source (1253.6 eV) and a pass energy of 160 eV for survey spectra and 20 eV for high-resolution spectra was measured at the Instituto de Nanociencia de Aragon (INA), Zaragoza, Spain. To compensate charging effects, all spectra were calibrated with respect to the C(1s) peak at 284.9 eV.

2.3.5. Electrical Characterization. In order to perform electrical measurements, 10 nm thick Pt contacts were ex situ deposited using a dc sputtering via a shadow mask forming an array of contacts of about 50 × 50 μm^2 each. Hence, the obtained metal films have the transparency of about 30% within the used range of laser wavelengths. The ferroelectric characterization was performed at room temperature using an aixACCT TFAnalizer2000 system with a virtual ground method. The voltage is applied to the top Pt electrode, whereas the bottom LSMO electrode is grounded. Ferroelectric loops were recorded using a triangular voltage waveform and the dynamic leakage current compensation method[50] at the frequency of 2 kHz, after being precycled 10 000 times. The photoresponse was induced using a blue sky research STEC multiwavelength system with a fixed parallel laser beam set at 44° angle to the sample surface. The available wavelengths were λ = 405, 450, 520, and 638 nm, whereas the power density was varied and mentioned in the text. The photoresponse versus time was measured using the TFAnalizer2000, whereas the I−V data were recorded using the Keithley 2600B sourcemeter. EQE measurements were performed with a supercontinuum white laser (Fiannium PM-SC) and a monochromator (Fiannium LLTF Contrast Vis-2), both from Photon ETC. To electrically measure the cell, a Keithley 2450 Sourcemeter was used alongside a LabView 2015 programme to control all the pieces of the equipment and collect the data. An optical fiber was connected to the output of the monochromator, and the other end was pointed toward the sample. After that, the sample was illuminated with a range of frequencies, and the short-circuit current was measured.

3. RESULTS AND DISCUSSION

3.1. Structure of Solution-Processed BFCO Films.
Solution-processed films obtained from nitrate precursors upon annealing result in pure phase and epitaxial (00l) BFCO for a range of cobalt substitutions starting from $x = 0$ to $x = 0.3$ (see the Supporting Information, Figure S1). High-resolution XRD RSMs for 20 nm pure BFO and BFCO with the maximum cobalt load ($x = 0.3$) (Figure 1) show two
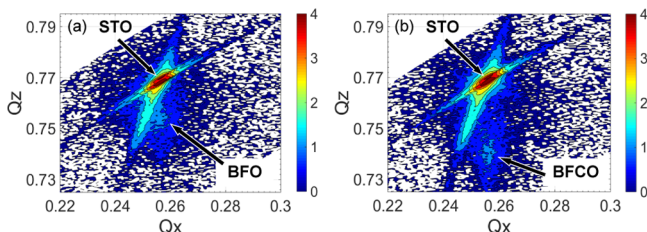

Figure 1. RSM around the (103) STO reflection for (a) BFO and (b) BFCO $x = 0.3$ thin films.

diffraction spots. The most intense one corresponds to (103) STO and the weaker one corresponds to the (103) BFCO film, confirming a heteroepitaxial growth. From the position of these spots, the lattice constants of the films have been extracted based on a pseudocubic symmetry. The in-plane lattice constant of both films exactly matches that of the STO substrate ($a = 3.905$ Å), whereas the out-of-plane lattice constant increases from $c = 3.976$ Å for BFO to $c = 4.047$ Å for BFCO with $x = 0.3$. When increasing the film thickness, the lattice parameter monotonously changes reaching $a = 3.953$ Å and $c = 3.985$ Å for 100 nm BFCO with $x = 0.3$. Lattice constants for bulk BFCO system are reported for $x = 0.1$ and $x = 0.2$ ($a \approx 3.95$ Å) and for $x = 0.4$ ($a \approx 3.75$ Å).[51] No experimental data are available for bulk BFCO $x = 0.3$. The dramatic lattice constant change between $x = 0.2$ and $x = 0.4$ is attributed to a phase transition. Thus, according to these values, it is likely that our films with $x = 0.3$ did not undergo a phase transition. Further cobalt incorporation ($x > 0.3$ to $x < 0.9$) enables epitaxial (00l) BFCO stabilization, although segregated secondary phases are visible (see the Supporting Information, Figure S1). This is in good agreement with the reported difficulty to stabilize BFO with high cobalt content without employing high-pressure synthesis.[47,52]

The crystalline quality of these two CSD-BFCO compositions was further investigated by STEM. This imaging mode provides images where the intensity scales with the square of the atomic number, referred to as Z-contrast images. Figure 2 shows a comparison of a Z-contrast image of 20 nm BFO and BFCO ($x = 0.3$) thin films. Both images show coherent epitaxial films' growth with a sharp interface with STO. BFCO films with $x > 0.3$ can present secondary phases at the film surface in agreement with XRD data (see Figure S2). The EEL spectrum acquired from the BFCO film shows the O K, Fe L, and Co L-edges, confirming the presence of cobalt within the BFCO film's structure.

3.2. Optical Properties of Solution-Processed BFCO Films.
The optical properties of the BFCO films were investigated by variable angle SE (Figure 3). Experimental data were fitted using the Tauc−Lorentz model (see Experimental Section and Figure S3). This study enabled to extract for the first time the complex refractive index (n and k) for the BFCO system. From the optical absorption coefficient
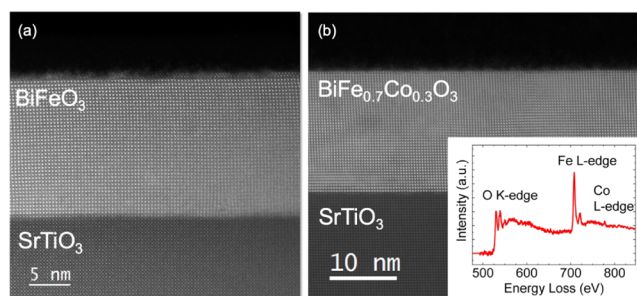

Figure 2. High-magnification Z-contrast images of (001)-oriented (a) BFO and (b) BFCO $x = 0.3$ on (100) STO substrates viewed along the [100]-crystallographic direction. Inset: background-subtracted EEL spectrum, extracted from a line scan spectrum image across the thickness of the film, showing the O K, Fe L, and Co L-edges.

(α) dependence with photon energy (Figure 3b), it is found that the absorption edge monotonously shifts to lower energies when increasing the Co content. Indeed, for $x = 0.3$, the absorption edge is at about 1.5 eV, well below the corresponding edge of pristine BFO films and in good agreement with the theoretical data of the transition metal-substituted BFO.[53]

Assuming a direct band gap for all the BFCO compositions, the optical band gap has been extracted from a linear extrapolation of $(\alpha E)^2$ to zero and from this extrapolation, a red shift is observed from 2.7 ± 0.1 eV for pure BFO to 2.3 ± 0.1 eV for BFCO with $x = 0.3$ (Figure S4). This is the largest band gap variation observed so far in BFO thin films by Co substitution.[44,46,53]

Figure 3c shows the extracted indices of refraction (n), indicating a ca 10% higher n for BFO and BFCO compared to the STO substrate. Pure BFO shows two spectral features at ~2.8 and ~4 eV that are linked to an absorption band peaking at an intermediate energy (Kramers−Kronig consistency). Previous SE investigations in unsubstituted BFO assigned these features to charge-transfer transitions (M 3d−O 2p and M 3d−M 3d).[31,54] The incorporation of cobalt slightly modifies the intensity and position of these two spectral features being more pronounced for BFCO with $x = 0.3$.[50,51] Additional features are also seen in absorption and in n at lower energies, in agreement with the aforementioned decrease in the band gap. The modifications observed in the BFCO spectra are believed to indicate that the metal-oxygen and metal−metal bonds have been altered upon cobalt substitution and consequently affect the band gap.[29,43,53]

3.3. Electrical Response of Solution-Processed BFCO Vertical Devices.
Figure 4 shows the ferroelectric hysteresis loops ($P−E$) of ~100 nm epitaxial BFCO thin films with $x = 0$, $x = 0.1$, and $x = 0.3$ prepared on (001)LSMO//STO and recorded in dark. Importantly, the $P−E$ loops were also recorded under illumination and overlap those acquired in dark, ruling out the effects of photogenerated charges on polarization.[55] The shape of the ferroelectric loop at high applied electric fields is not well saturated due to the residual contribution of the leakage current.[56,57] The measured remnant polarization (P_r) and coercive field (E_c) for pure BFO films are 26.1 μC cm^{-2} and 182 kV cm^{-1}, respectively, being in agreement with previous reports of epitaxial CSD-BFO films.[40,58,59] Substitution of cobalt leads to enhanced $P_r \approx$ 60 μC cm^{-2} (50% increase) and larger $E_c = 600$ kV cm^{-1} ($x = 0.1$) and 373 kV cm^{-1} ($x = 0.3$). It has been demonstrated that
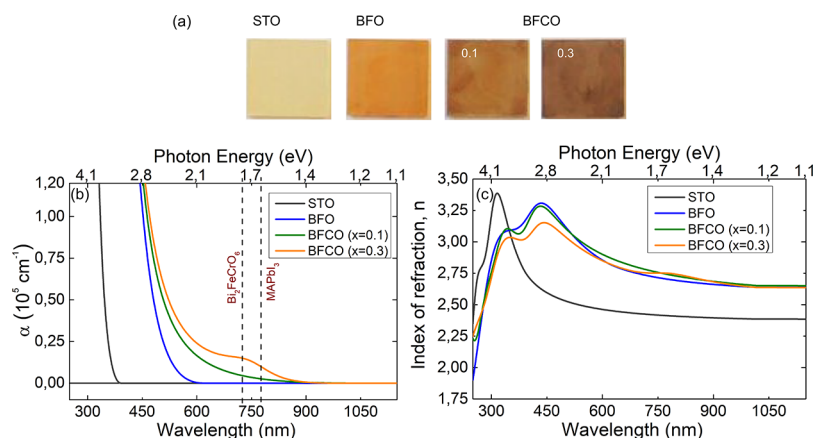
Figure 3. (a) Optical microscopy images of the STO substrate, BFO, and BFCO samples. (b) Absorption coefficient, α, as a function of photon energy of BFCO thin films ($x = 0$ to $x = 0.3$) compared to STO. Bi_2FeCrO_6 and $MAPbI_3$ (MA = methylammonium) band gaps are indicated with dashed lines for comparison. (c) Corresponding indices of refraction (n).
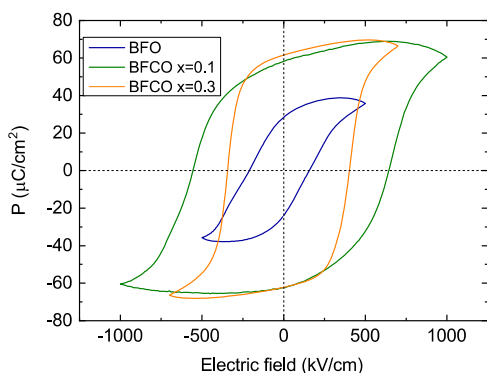

Figure 4. Ferroelectric hysteresis $P-E$ recorded at 2 kHz at room temperature for BFO and BFCO thin films with different cobalt contents.

lattice deformation in ferroelectric films such as $BaTiO_3$ can impact the magnitude of the polarization.[60,61] Similarly, here it is suggested that the incorporation of cobalt will promote lattice deformation enhancing the ferroelectric response.

Photoresponse measurements have been carried out for BFO, as well as BFCO with $x = 0.1$ and $x = 0.3$. The samples have been measured with the contact configuration shown in Figure 5a. Here, we define the positive sign of the current (J), where positive carriers flow from the top Pt electrode to the bottom LSMO electrode (ground), as indicated by the arrows. $I-V$ curves have been collected after applying prepoling voltages being different for each composition according to their ferroelectric coercive field found in the $P(E)$ loops (Figure 4), namely, ± 3 V for BFO, ± 5 V for BFCO $x = 0.1$, and ± 7 V for BFCO $x = 0.3$ (Figure 5b). The observed linear $J-V$ dependence is rather common in many ferroelectric
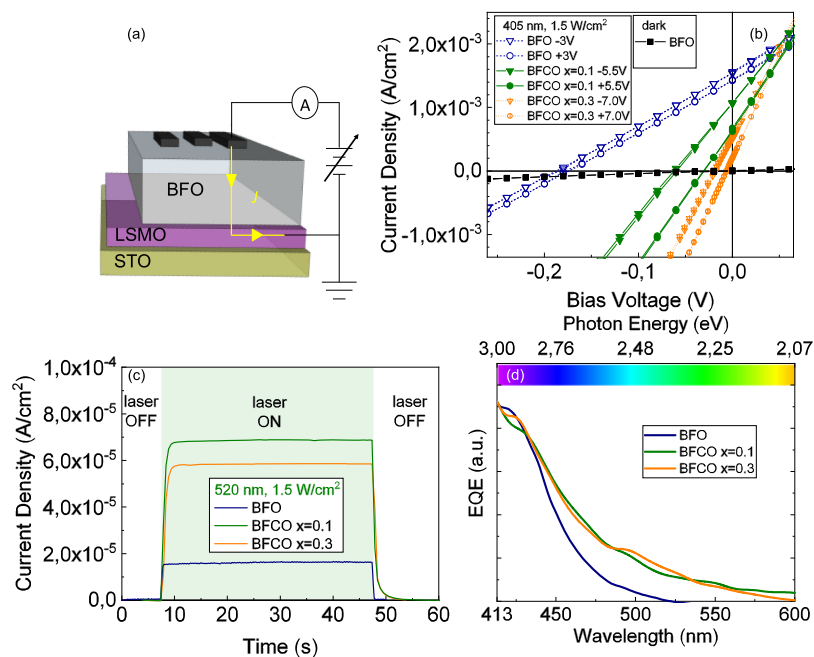

Figure 5. (a) Scheme of the electrical configuration used to measure the photoresponse, (b) $J-V$ curves for BFO and BFCO positively and negatively poled films illuminated under 405 nm, 1.5 W cm^{-2}. (c) Time dependence of the short-circuit photocurrent for BFO and BFCO $x = 0.1$ and $x = 0.3$ films illuminated under 520 nm with a laser of 1.5 W cm^{-2}. (d) EQE.

perovskite oxides and contrasts with the rectifying behavior of high-performance solar cells.[5,15,62] This characteristic can be related to the dominant conduction mechanism that will be discussed below.

Illuminating the BFO sample with a 405 nm wavelength laser and 1.5 W cm^{-2} intensity (below BFO band gap energy) causes a drastic change in the $I-V$ curve. The resulting short-circuit current and open-circuit voltage are J_{sc} = 1.56 mA cm^{-2} and V_{oc} = −186 mV, respectively. The V_{oc} is similar to those reported in the high-quality PLD BFO/LSMO//STO system.[63] Note that the negative V_{oc} values irrespective of the prepoling applied voltage result from the asymmetric device structure. Illuminating the cobalt-substituted BFO films with the same 405 nm wavelength laser results in average J_{sc} values of 1.07 mA cm^{-2} (x = 0.1) and 0.4 mA cm^{-2} (x = 0.3) and V_{oc} values of −61 mV (x = 0.1) and −13 mV (x = 0.3) evidencing that both J_{sc} and V_{oc} decrease with the incorporation of cobalt. The decrease in J_{sc} is assigned to an increased leakage current observed when increasing the cobalt doping (see Figure S5) as well as a small reduction in absorption coefficient at this excitation wavelength (see Figure S4). On the other hand, the decrease in V_{oc} may be due to a combination of factors including increased charge recombination due to defects, decrease in photocurrent, and lowering the band gap. Importantly, the magnitude of J_{sc} and V_{oc} can be modulated by applying a voltage of a particular polarity. This effect is stronger in BFCO compared to that in pristine BFO, consistent with the higher value of (switchable) remnant polarization seen in Figure 4. The different magnitude of the photocurrent observed for the same sample under different signs of the applied voltage indicates the presence of two remnant states.[5,64]

Then, the photoresponse of the samples BFO, BFCO x = 0.1, and BFCO x = 0.3 can be compared when illuminated with a laser of 520 nm (below the tuned band gap energy upon cobalt substitution) and without being prepolarized (Figure 5c). The J_{sc} of BFCO is larger by a factor of four compared to that of unsubstituted BFO, which is in agreement with the band gap decrease observed by the incorporation of Co. When comparing the BFCO samples with different cobalt additions, the sample with Co x = 0.3 shows slightly lower photocurrent than the sample with Co x = 0.1. This could be attributed to the higher leakage currents in x = 0.3 as mentioned above (Figure S5). Finally, the EQE measurements further confirm that BFCO films exhibit an enhanced photocurrent, hence a higher photoresponse, compared to unsubstituted BFO between 440 and 590 nm (Figure 5d). Incident photon to charge carrier efficiency (IPCE) for BFCO films at 520 nm and 100 mW cm^{-2} is still low (0.02%); however, it is one order of magnitude higher than pristine BFO (<0.003%).

It is well-known that BFO shows larger leakage currents compared to other perovskite oxides.[65,66] We have evaluated the dominant conduction mechanism by analyzing the $J-E$ characteristics at room temperature (see Figure S5b). From the linear dependence in the log J–log E plot, the data can be fitted with a slope close to 1 suggesting that in our working conditions, that is under ∼30 kV/cm, the dominant mechanism most likely is the Ohmic conduction (bulk-limited).[67,68] In fact, former studies on epitaxial BFO films have reported that the most common conduction mechanisms are bulk-limited (space-charge-limited current and Poole–Frenkel emission), although interface effects cannot be neglected.[65,69] Note that improved devices based on BFO

can show the typical rectifying behavior in structures such as Pt/BFO/SrRuO$_3$/STO.[19] The leakage current in BFO films is mainly attributed to deviations in oxygen stoichiometry and Fe^{3+} to Fe^{2+} transition.[70−72] XPS analysis has been performed in order to investigate the surface chemistry of BFO and BFCO films with x = 0.3 (see Figure S6). From the Fe 2p core-level spectra, it is suggested that the predominant specie in all the films are Fe^{3+}. From the Co 2p core-level spectrum, the coexistence of Co^{3+} and Co^{2+} is suggested. Because no Co-rich secondary phases are identified in the structural analysis (i.e., Co$_3$O$_4$, CoFe$_2$O$_4$), the presence of Co^{2+} is very likely to be compensated by the formation of oxygen vacancies, which could contribute to the Ohmic conduction identified above.

Clearly, boosting the efficiency in this system is still a challenge and requires further investigation. Future steps to unlock the full potential of the BFCO-based PV device might be achieved through optimizing microstructures (porosity and surface precipitates) of the active material,[59,73,74] performing A-site cosubstitution and oxygen annealing to minimize fluctuations of the oxygen stoichiometry,[75−79] and performing interface engineering through the incorporation of selective layers[80−82] and transparent oxide electrodes[83] to facilitate charge collection and extraction.

4. CONCLUSIONS

In this work, we have demonstrated the viability of solution processing to stabilize BFCO films by epitaxial growth. The incorporation of cobalt up to x = 0.3 allows a band gap modulation from 2.7 to 2.3 eV while showing large ferroelectricity. The photocurrent response has been evaluated using a relatively simple device geometry pursuing an oxide-based heterostructure, Pt/BFCO/LSMO//STO. Upon cobalt incorporation, the photocurrent is enhanced according to the band gap narrowing, although EQE is, however, still low compared to state-of-the-art ferroelectric perovskite oxides. Further elemental chemical substitution investigations together with interfacial engineering should be performed to increase the efficiency. Overall, the BFCO system is a potential photoactive material, and we believe it will provide a robust platform to study the underlying physical properties of these systems such as the correlation between cation substitution and optical and electronic properties. The field of ferroelectric perovskite oxides is young and dynamic and is expected to contribute toward a stable, robust, and efficient photovoltaic (all-oxide) device . The band gap tuning possibilities could also offer new opportunities when combined with other conventional photovoltaic devices.

■ ASSOCIATED CONTENT

ⓢ Supporting Information

The Supporting Information is available free of charge on the ACS Publications website at DOI: 10.1021/acs.chemmater.8b04380.

> Additional XRD $\theta-2\theta$ scans; AFM topographic images and n and k refractive index for BFCO with x = 0 to x = 0.9 thin films; table of calculated c parameters; STEM image of BFCO x > 0.3; leakage curves for BFO, BFCO x = 0.1, and x = 0.3; XPS spectra of BFO and BFCO x = 0.3; XRD and AFM of optimized BFO/LSMO//STO films; and current density and IPCE versus laser photon energy of BFO films (PDF)

■ **AUTHOR INFORMATION**

Corresponding Author
*E-mail: mcoll@icmab.es.

ORCID ●
Mariona Coll: 0000-0001-5157-7764

Author Contributions
The manuscript was written through contributions of all authors. All authors have given approval to the final version of the manuscript.

Notes
The authors declare no competing financial interest.

■ **REFERENCES**

(1) Rühle, S.; Anderson, A. Y.; Barad, H.-N.; Kupfer, B.; Bouhadana, Y.; Rosh-Hodesh, E.; Zaban, A. All-Oxide Photovoltaics. *J. Phys. Chem. Lett.* **2012**, *3*, 3755−3764.

(2) Pérez-Tomás, A.; Mingorance, A.; Tanenbaum, D.; Lira-Cantú, M. Metal Oxides in Photovoltaics: All-Oxide, Ferroic, and Perovskite Solar Cells A2—Lira-Cantu, Monica BT—The Future of Semiconductor Oxides in Next-Generation Solar Cells. *Metal Oxides*; Elsevier, 2018; Chapter 8, pp 267−356.

(3) Barquinha, P.; Martins, R.; Pereira, L.; Fortunato, E. Transparent Oxide Electronics. *Transparent Oxide Electronics*; Wiley Online Books, 2012.

(4) Coll, M.; Fontcuberta, J.; Althammer, M.; Gross, R.; Grollier, J.; Bibes, M.; Garcia, V.; Boschker, H.; Mannhart, J.; Calleja, A.; et al. Towards Oxide Electronics: A Roadmap. *Appl. Surf. Sci.* **2019**, DOI: 10.1016/j.apsusc.2018.09.294.

(5) Lopez-Varo, P.; Bertoluzzi, L.; Bisquert, J.; Alexe, M.; Coll, M.; Huang, J.; Jimenez-Tejada, J. A.; Kirchartz, T.; Nechache, R.; Rosei, F.; et al. Physical Aspects of Ferroelectric Semiconductors for Photovoltaic Solar Energy Conversion. *Phys. Rep.* **2016**, *653*, 1−40.

(6) Paillard, C.; Bai, X.; Infante, I. C.; Guennou, M.; Geneste, G.; Alexe, M.; Kreisel, J.; Dkhil, B. Photovoltaics with Ferroelectrics: Current Status and Beyond. *Adv. Mater.* **2016**, *28*, 5153−5168.

(7) Butler, K. T.; Frost, J. M.; Walsh, A. Ferroelectric Materials for Solar Energy Conversion: Photoferroics Revisited. *Energy Environ. Sci.* **2015**, *8*, 838−848.

(8) Li, W.; Ji, L.-J. Perovskite Ferroelectrics Go Metal Free. *Science* **2018**, *361*, 132.

(9) Park, N.-G.; Grätzel, M.; Miyasaka, T.; Zhu, K.; Emery, K. Towards Stable and Commercially Available Perovskite Solar Cells. *Nat. Energy* **2016**, *1*, 16152.

(10) Bisquert, J.; Qi, Y.; Ma, T.; Yan, Y. Advances and Obstacles on Perovskite Solar Cell Research from Material Properties to Photovoltaic Function. *ACS Energy Lett.* **2017**, *2*, 520−523.

(11) National Renewable Energy Laboratory (NREL). https://www.nrel.gov/pv/assets/pdfs/pv-efficiency-chart.20181221.pdf, accessed 14/01/2019.

(12) Rappe, A. M.; Grinberg, I.; Spanier, J. E. Getting a Charge out of Hybrid Perovskites. *Proc. Natl. Acad. Sci. U.S.A.* **2017**, *114*, 7191−7193.

(13) Coll, M.; Gomez, A.; Mas-Marza, E.; Almora, O.; Garcia-Belmonte, G.; Campoy-Quiles, M.; Bisquert, J. Polarization Switching and Light-Enhanced Piezoelectricity in Lead Halide Perovskites. *J. Phys. Chem. Lett.* **2015**, *6*, 1408−1413.

(14) Yang, M.; Bhatnagar, A.; Alexe, M. Electronic Origin and Tailoring of Photovoltaic Effect in $BiFeO_3$ Single Crystals. *Adv. Electron. Mater.* **2015**, *1*, 1500139.

(15) Bhatnagar, A.; Roy Chaudhuri, A.; Heon Kim, Y.; Hesse, D.; Alexe, M. Role of Domain Walls in the Abnormal Photovoltaic Effect in $BiFeO_3$. *Nat. Commun.* **2013**, *4*, 2835.

(16) Kim, D. J.; Alexe, M. Bulk Photovoltaic Effect in Monodomain $BiFeO_3$ Thin Films. *Appl. Phys. Lett.* **2017**, *110*, 183902.

(17) Spanier, J. E.; Fridkin, V. M.; Rappe, A. M.; Akbashev, A. R.; Polemi, A.; Qi, Y.; Gu, Z.; Young, S. M.; Hawley, C. J.; Imbrenda, D.; et al. Power conversion efficiency exceeding the Shockley-Queisser limit in a ferroelectric insulator. *Nat. Photonics* **2016**, *10*, 611.

(18) Alexe, M.; Hesse, D. Tip-Enhanced Photovoltaic Effects in Bismuth Ferrite. *Nat. Commun.* **2011**, *2*, 256.

(19) Lee, D.; Baek, S. H.; Kim, T. H.; Yoon, J.-G.; Folkman, C. M.; Eom, C. B.; Noh, T. W. Polarity Control of Carrier Injection at Ferroelectric/Metal Interfaces for Electrically Switchable Diode and Photovoltaic Effects. *Phys. Rev. B: Condens. Matter Mater. Phys.* **2011**, *84*, 125305.

(20) Bretos, I.; Jiménez, R.; Ricote, J.; Calzada, M. L. Synthesis by Low Temperature Solution Processing of Ferroelectric Perovskite Oxide Thin Films as Candidate Materials for Photovoltaic Applications A2—Lira-Cantu, Monica BT—The Future of Semiconductor Oxides in Next-Generation Solar Cells. *Metal Oxides*; Elsevier, 2018; Chapter 2, pp 45−81.

(21) Yang, S. Y.; Seidel, J.; Byrnes, S. J.; Shafer, P.; Yang, C.-H.; Rossell, M. D.; Yu, P.; Chu, Y.-H.; Scott, J. F.; Ager, J. W., III; et al. Above-Bandgap Voltages from Ferroelectric Photovoltaic Devices. *Nat. Nanotechnol.* **2010**, *5*, 143.

(22) Bhatnagar, A.; Kim, Y. H.; Hesse, D.; Alexe, M. Persistent Photoconductivity in Strained Epitaxial $BiFeO_3$ Thin Films. *Nano Lett.* **2014**, *14*, 5224−5228.

(23) Wang, F.; Grinberg, I.; Jiang, L.; Young, S. M.; Davies, P. K.; Rappe, A. M. Materials Design of Visible-Light Ferroelectric Photovoltaics from First Principles. *Ferroelectrics* **2015**, *483*, 1−12.

(24) Arima, T.; Tokura, Y.; Torrance, J. B. Variation of optical gaps in perovskite-type 3d transition-metal oxides. *Phys. Rev. B: Condens. Matter Mater. Phys.* **1993**, *48*, 17006−17009.

(25) Wang, J.; Neaton, J. B.; Zheng, H.; Nagarajan, V.; Ogale, S. B.; Liu, B.; Viehland, D.; Vaithyanathan, V.; Schlom, D. G.; Waghmare, U. V.; et al. Epitaxial $BiFeO_3$ Multiferroic Thin Film Heterostructures. *Science* **2003**, *299*, 1719−1722.

(26) Kumar, A.; Rai, R. C.; Podraza, N. J.; Denev, S.; Ramirez, M.; Chu, Y.-H.; Martin, L. W.; Ihlefeld, J.; Heeg, T.; Schubert, J.; et al. Linear and Nonlinear Optical Properties of $BiFeO_3$. *Appl. Phys. Lett.* **2008**, *92*, 121915.

(27) Leguy, A. M. A.; Azarhoosh, P.; Alonso, M. I.; Campoy-Quiles, M.; Weber, O. J.; Yao, J.; Bryant, D.; Weller, M. T.; Nelson, J.; Walsh, A.; et al. Experimental and Theoretical Optical Properties of Methylammonium Lead Halide Perovskites. *Nanoscale* **2016**, *8*, 6317−6327.

(28) Pettersson, L. A. A.; Roman, L. S.; Inganäs, O. Modeling Photocurrent Action Spectra of Photovoltaic Devices Based on Organic Thin Films. *J. Appl. Phys.* **1999**, *86*, 487−496.

(29) Wang, F.; Grinberg, I.; Rappe, A. M. Band Gap Engineering Strategy via Polarization Rotation in Perovskite Ferroelectrics. *Appl. Phys. Lett.* **2014**, *104*, 152903.

(30) Herklotz, A.; Rus, S. F.; Ward, T. Z. Continuously Controlled Optical Band Gap in Oxide Semiconductor Thin Films. *Nano Lett.* **2016**, *16*, 1782−1786.

(31) Sando, D.; Carrétéro, C.; Grisolia, M. N.; Barthélémy, A.; Nagarajan, V.; Bibes, M. Revisiting the Optical Band Gap in Epitaxial BiFeO₃ Thin Films. *Adv. Opt. Mater.* **2018**, *6*, 1700836.

(32) Zhang, Y.; Sahoo, M. P. K.; Wang, J. Tuning the Band Gap and Polarization of BaSnO₃/SrSnO₃ Superlattices for Photovoltaic Applications. *Phys. Chem. Chem. Phys.* **2017**, *19*, 7032−7039.

(33) Grinberg, I.; West, D. V.; Torres, M.; Gou, G.; Stein, D. M.; Wu, L.; Chen, G.; Gallo, E. M.; Akbashev, A. R.; Davies, P. K.; et al. Perovskite Oxides for Visible-Light-Absorbing Ferroelectric and Photovoltaic Materials. *Nature* **2013**, *503*, 509.

(34) Bai, Y.; Tofel, P.; Palosaari, J.; Jantunen, H.; Juuti, J. A Game Changer: A Multifunctional Perovskite Exhibiting Giant Ferroelectricity and Narrow Bandgap with Potential Application in a Truly Monolithic Multienergy Harvester or Sensor. *Adv. Mater.* **2017**, *29*, 1700767.

(35) Cao, J.; Ji, Y.; Tian, C.; Yi, Z. Synthesis and enhancement of visible light activities of nitrogen-doped BaTiO₃. *J. Alloys Compd.* **2014**, *615*, 243−248.

(36) Nechache, R.; Harnagea, C.; Li, S.; Cardenas, L.; Huang, W.; Chakrabartty, J.; Rosei, F. Bandgap Tuning of Multiferroic Oxide Solar Cells. *Nat. Photonics* **2014**, *9*, 61.

(37) Chakrabartty, J.; Harnagea, C.; Celikin, M.; Rosei, F.; Nechache, R. Improved Photovoltaic Performance from Inorganic Perovskite Oxide Thin Films with Mixed Crystal Phases. *Nat. Photonics* **2018**, *12*, 271−276.

(38) Vila-Fungueiriño, J. M.; Rivas-Murias, B.; Rubio-Zuazo, J.; Carretero-Genevrier, A.; Lazzari, M.; Rivadulla, F. Polymer Assisted Deposition of Epitaxial Oxide Thin Films. *J. Mater. Chem. C* **2018**, *6*, 3834−3844.

(39) Coll, M.; Gàzquez, J.; Huhne, R.; Holzapfel, B.; Morilla, Y.; García-López, J.; Pomar, A.; Sandiumenge, F.; Puig, T.; Obradors, X. All chemical YBa₂Cu₃O₇ superconducting multilayers: Critical role of CeO₂ cap layer flatness. *J. Mater. Res.* **2009**, *24*, 1446−1455.

(40) Zhang, Q.; Valanoor, N.; Standard, O. Epitaxial (001) BiFeO₃ Thin-Films with Excellent Ferroelectric Properties by Chemical Solution Deposition-the Role of Gelation. *J. Mater. Chem. C* **2015**, *3*, 582−595.

(41) Singh, S. K.; Kim, Y. K.; Funakubo, H.; Ishiwara, H. Epitaxial BiFeO₃ Thin Films Fabricated by Chemical Solution Deposition. *Appl. Phys. Lett.* **2006**, *88*, 162904.

(42) Diéguez, O.; Íñiguez, J. First-Principles Investigation of Morphotropic Transitions and Phase-Change Functional Responses in BiFeO₃-BiCoO₃ Multiferroic Solid Solutions. *Phys. Rev. Lett.* **2011**, *107*, 057601.

(43) Wulfsberg, G. *Inorganic Chemistry*; University Science Books: California, 2000.

(44) Peng, L.; Deng, H.; Tian, J.; Ren, Q.; Peng, C.; Huang, Z.; Yang, P.; Chu, J. Influence of Co doping on structural, optical and magnetic properties of BiFeO₃ films deposited on quartz substrates by sol-gel method. *Appl. Surf. Sci.* **2013**, *268*, 146−150.

(45) Xue, X.; Tan, G.; Liu, W.; Hao, H. Structural, optical and magnetic properties of BiFe₁₋ₓCoₓO₃ thin films. *Mater. Lett.* **2014**, *128*, 303−305.

(46) Shima, H.; Nishida, K.; Yamamoto, T.; Tadokoro, T.; Tsutsumi, K.; Suzuki, M.; Naganuma, H. Large Refractive Index in BiFeO₃-BiCoO₃ Epitaxial Films. *J. Appl. Phys.* **2013**, *113*, 17A914.

(47) Belik, A. A.; Iikubo, S.; Kodama, K.; Igawa, N.; Shamoto, S.-i.; Niitaka, S.; Azuma, M.; Shimakawa, Y.; Takano, M.; Izumi, F.; et al. Neutron Powder Diffraction Study on the Crystal and Magnetic Structures of BiCoO₃. *Chem. Mater.* **2006**, *18*, 798−803.

(48) Yasui, S.; Nishida, K.; Naganuma, H.; Okamura, S.; Iijima, T.; Funakubo, H. Crystal Structure Analysis of Epitaxial BiFeO₃ −BiCoO₃ Solid Solution Films Grown by Metalorganic Chemical Vapor Deposition. *Jpn. J. Appl. Phys.* **2007**, *46*, 6948.

(49) Coll, M.; Palau, A.; Gonzalez-Rosillo, J. C.; Gazquez, J.; Obradors, X.; Puig, T. Integration of atomic layer deposition CeO₂

thin films with functional complex oxides and 3D patterns. *Thin Solid Films* **2014**, *553*, 7−12.

(50) Meyer, R.; Waser, R.; Prume, K.; Schmitz, T.; Tiedke, S. Dynamic Leakage Current Compensation in Ferroelectric Thin-Film Capacitor Structures. *Appl. Phys. Lett.* **2005**, *86*, 142907.

(51) Azuma, M.; Niitaka, S.; Hayashi, N.; Oka, K.; Takano, M.; Funakubo, H.; Shimakawa, Y. Rhombohedral−Tetragonal Phase Boundary with High Curie Temperature in (1- x)BiCoO₃ − x BiFeO₃ Solid Solution. *Jpn. J. Appl. Phys.* **2008**, *47*, 7579.

(52) Yasui, S.; Naganuma, H.; Okamura, S.; Nishida, K.; Yamamoto, T.; Iijima, T.; Azuma, M.; Morioka, H.; Saito, K.; Ishikawa, M.; et al. Crystal Structure and Electrical Properties of {100}-Oriented Epitaxial BiCoO₃-BiFeO₃ Films Grown by Metalorganic Chemical Vapor Deposition. *Jpn. J. Appl. Phys.* **2008**, *47*, 7582−7585.

(53) Qiao, L.; Zhang, S.; Xiao, H. Y.; Singh, D. J.; Zhang, K. H. L.; Liu, Z. J.; Zu, X. T.; Li, S. Orbital controlled band gap engineering of tetragonal BiFeO₃ for optoelectronic applications. *J. Mater. Chem. C* **2018**, *6*, 1239−1247.

(54) Pisarev, R. V.; Moskvin, A. S.; Kalashnikova, A. M.; Rasing, T. Charge Transfer Transitions in Multiferroic BiFeO₃ and Related Ferrite Insulators. *Phys. Rev. B: Condens. Matter Mater. Phys.* **2009**, *79*, 235128.

(55) Dimos, D.; Potter, B. G.; Sinclair, M. B.; Tuttle, B. A.; Warren, W. L. Photo-induced and electrooptic properties of (Pb,La)(Zr,Ti)O₃ films for optical memories. *Integr. Ferroelectr.* **1994**, *5*, 47−58.

(56) Yan, H.; Inam, F.; Viola, G.; Ning, H.; Zhang, H.; Jiang, Q.; Zeng, T.; Gao, Z.; Reece, M. J. The Contribution of Electrical Conductivity, Dielectric Permittivity and Domain Switching in Ferroelectric Hysteresis Loops. *J. Adv. Dielectr.* **2011**, *01*, 107−118.

(57) Fina, I.; Fàbrega, L.; Langenberg, E.; Martí, X.; Sánchez, F.; Varela, M.; Fontcuberta, J. Nonferroelectric Contributions to the Hysteresis Cycles in Manganite Thin Films: A Comparative Study of Measurement Techniques. *J. Appl. Phys.* **2011**, *109*, 074105.

(58) *Chemical Solution Deposition of Functional Oxide Thin Films*; Schneller, T., Waser, R., Kosec, M., Payne, D., Eds.; Springer: Vienna: Viena, 2013.

(59) Casper, M. D.; Losego, M. D.; Maria, J.-P. Optimizing Phase and Microstructure of Chemical Solution-Deposited Bismuth Ferrite (BiFeO₃) Thin Films to Reduce DC Leakage. *J. Mater. Sci.* **2012**, *48*, 1578−1584.

(60) Khestanova, E.; Dix, N.; Fina, I.; Scigaj, M.; Rebled, J. M.; Magén, C.; Estradé, S.; Peiró, F.; Herranz, G.; Fontcuberta, J.; et al. Untangling Electrostatic and Strain Effects on the Polarization of Ferroelectric Superlattices. *Adv. Funct. Mater.* **2016**, *26*, 6446−6453.

(61) Damodaran, A. R.; Breckenfeld, E.; Chen, Z.; Lee, S.; Martin, L. W. Enhancement of Ferroelectric Curie Temperature in BaTiO₃ Films via Strain-Induced Defect Dipole Alignment. *Adv. Mater.* **2014**, *26*, 6341−6347.

(62) Zenkevich, A.; Matveyev, Y.; Maksimova, K.; Gaynutdinov, R.; Tolstikhina, A.; Fridkin, V. Giant Bulk Photovoltaic Effect in Thin Ferroelectric BaTiO₃ Films. *Phys. Rev. B: Condens. Matter Mater. Phys.* **2014**, *90*, 161409.

(63) Yang, Y.; Xu, W.; Xu, X.; Wang, Y.; Yuan, G.; Wang, Y.; Liu, Z. The enhanced photocurrent of epitaxial BiFeO₃ film at 130 °C. *J. Appl. Phys.* **2016**, *119*, 044102.

(64) Lu, Z.; Li, P.; Wan, J.-g.; Huang, Z.; Tian, G.; Pan, D.; Fan, Z.; Gao, X.; Liu, J.-m. Controllable Photovoltaic Effect of Microarray Derived from Epitaxial Tetragonal BiFeO₃ Films. *ACS Appl. Mater. Interfaces* **2017**, *9*, 27284−27289.

(65) Pintilie, L. *Charge Transport in Ferroelectric Thin Films*; INTECH Open Access Publisher, 2011; Chapter 5, pp 101−134.

(66) Pintilie, L.; Alexe, M. Metal-Ferroelectric-Metal Heterostructures with Schottky Contacts. I. Influence of the Ferroelectric Properties. *J. Appl. Phys.* **2005**, *98*, 124103.

(67) Sigov, A.; Podgorny, Y.; Vorotilov, K.; Vishnevskiy, A. Leakage Currents in Ferroelectric Thin Films. *Phase Transitions* **2013**, *86*, 1141−1151.

(68) Wu, J.; Wang, J.; Xiao, D.; Zhu, J. Leakage Mechanism of Cation -Modified BiFeO₃ Thin Film. *AIP Adv.* **2011**, *1*, 022138.

(69) Pintilie, L.; Dragoi, C.; Chu, Y. H.; Martin, L. W.; Ramesh, R.; Alexe, M. Orientation-dependent potential barriers in case of epitaxial Pt-BiFeO$_3$-SrRuO$_3$ capacitors. *Appl. Phys. Lett.* **2009**, *94*, 232902.

(70) Wang, Y. P.; Zhou, L.; Zhang, M. F.; Chen, X. Y.; Liu, J.-M.; Liu, Z. G. Room-Temperature Saturated Ferroelectric Polarization in BiFeO$_3$ Ceramics Synthesized by Rapid Liquid Phase Sintering. *Appl. Phys. Lett.* **2004**, *84*, 1731−1733.

(71) Rojac, T.; Bencan, A.; Malic, B.; Tutuncu, G.; Jones, J. L.; Daniels, J. E.; Damjanovic, D. BiFeO$_3$ Ceramics: Processing, Electrical, and Electromechanical Properties. *J. Am. Ceram. Soc.* **2014**, *97*, 1993−2011.

(72) Dai, Z.; Akishige, Y. Electrical Properties of Multiferroic BiFeO$_3$ Ceramics Synthesized by Spark Plasma Sintering. *J. Phys. D: Appl. Phys.* **2010**, *43*, 445403.

(73) Shelke, V.; Harshan, V. N.; Kotru, S.; Gupta, A. Effect of Kinetic Growth Parameters on Leakage Current and Ferroelectric Behavior of BiFeO$_3$ Thin Films. *J. Appl. Phys.* **2009**, *106*, 104114.

(74) Nakamura, Y.; Nakashima, S.; Okuyama, M. Improvement of Ferroelectric Properties of BiFeO$_3$ Thin Films by Postmetallization Annealing and Electric Field Application. *J. Appl. Phys.* **2009**, *105*, 061616.

(75) Katiyar, R. K.; Sharma, Y.; Misra, P.; Puli, V. S.; Sahoo, S.; Kumar, A.; Scott, J. F.; Morell, G.; Weiner, B. R.; Katiyar, R. S. Studies of the Switchable Photovoltaic Effect in Co-Substituted BiFeO$_3$ Thin Films. *Appl. Phys. Lett.* **2014**, *105*, 172904.

(76) Zhou, H.-F.; Hou, Z.-L.; Kong, L.-B.; Jin, H.-B.; Cao, M.-S.; Qi, X. Enhanced Magnetization and Improved Leakage in Er-doped BiFeO$_3$ Nanoparticles. *Phys. Status Solidi A* **2013**, *210*, 809−813.

(77) Kuang, D.; Tang, P.; Yang, S.; Zhang, Y. Effects of Pr and Ni Co-Substitution on the Structural and Ferroelectric Properties of BiFeO$_3$ Thin Films Prepared by a Sol-Gel Method. *Ferroelectrics* **2015**, *488*, 97−103.

(78) You, L.; Zheng, F.; Fang, L.; Zhou, Y.; Tan, L. Z.; Zhang, Z.; Ma, G.; Schmidt, D.; Rusydi, A.; Wang, L.; et al. Enhancing Ferroelectric Photovoltaic Effect by Polar Order Engineering. *Sci. Adv.* **2018**, *4*, eaat3438.

(79) Go, H.-y.; Wakiya, N.; Funakubo, H.; Satoh, K.; Kondo, M.; Cross, J. S.; Maruyama, K.; Mizutani, N.; Shinozaki, K. Effect of Oxygen Annealing on Ferroelectricity of BiFeO$_3$ Thin Films Formed by Pulsed Laser Deposition. *Jpn. J. Appl. Phys.* **2007**, *46*, 3491.

(80) Wang, L.; Ma, H.; Chang, L.; Ma, C.; Yuan, G.; Wang, J.; Wu, T. Ferroelectric BiFeO$_3$ as an Oxide Dye in Highly Tunable Mesoporous All-Oxide Photovoltaic Heterojunctions. *Small* **2016**, *13*, 1602355.

(81) Li, S.; Chen, F.; Schafranek, R.; Bayer, T. J. M.; Rachut, K.; Fuchs, A.; Siol, S.; Weidner, M.; Hohmann, M.; Pfeifer, V.; et al. Intrinsic Energy Band Alignment of Functional Oxides. *Phys. Status Solidi RRL* **2014**, *8*, 571−576.

(82) Shirahata, Y.; Oku, T. Characterization and Photovoltaic Properties of BiFeO$_3$ Thin Films. *Coatings* **2016**, *6*, 68.

(83) Dong, W.; Guo, Y.; Guo, B.; Liu, H.; Li, H.; Liu, H. Photovoltaic Properties of BiFeO$_3$ Thin Film Capacitors by Using Al-Doped Zinc Oxide as Top Electrode. *Mater. Lett.* **2013**, *91*, 359−361.